MNRAS **000**, 1–9 (2018) Preprint 20 August 2019 Compiled using MNRAS LATEX style file v3.0

# The SAMI Galaxy Survey: The contribution of different kinematic classes to stellar mass function of nearby galaxies

Kexin Guo,[1,2]★ Luca Cortese,[2,5] Danail Obreschkow,[2,5] Barbara Catinella,[2,5] Jesse van de Sande, [3,5] and ...[4]

[1]*Kavli Institute for Astronomy and Astrophysics, Peking University, 5 Yiheyuan Road, Haidian District, Beijing 100871, P.R.China*
[2]*International Centre for Radio Astronomy Research (ICRAR), University of Western Australia, Crawley, WA 6009, Australia*
[3]*Sydney Institute for Astronomy, School of Physics, A28, The University of Sydney, NSW, 2006, Australia*
[4]*Another Department, Different Institution, Street Address, City Postal Code, Country*
[5]*ARC Centre of Excellence for All Sky Astrophysics in 3 Dimensions (ASTRO 3D),Australia*

Accepted XXX. Received YYY; in original form ZZZ

**ABSTRACT**

We use the complete Sydney-AAO Multi-object Integral field spectrograph (SAMI) Galaxy Survey to determine the contribution of slow rotators, as well as different types of fast rotators, to the stellar mass function of galaxies in the local Universe. We use stellar kinematics not only to discriminate between fast and slow rotators, but also to distinguish between dynamically cold systems (i.e., consistent with intrinsic axis ratios< 0.3) and systems including a prominent dispersion-supported bulge. We show that fast rotators account for more than 80% of the stellar mass budget of nearby galaxies, confirming that their number density overwhelms that of slow rotators at almost all masses. Most importantly, dynamically cold disks contribute to at least 25% of the stellar mass budget of the local Universe, significantly higher than what is estimated from visual morphology alone. For stellar masses up to $10^{10.5}M_{\odot}$, this class makes up >= 30% of the galaxy population in each stellar mass bin. The fact that many galaxies which are visually classified as two-components have stellar spin consistent with dynamically cold disks suggests that the inner component is either rotationally-dominated (e.g., bar, pseudo-bulge) or has little effect on the global stellar kinematics of galaxies.

**Key words:** galaxies: abundances – galaxies: kinematics and dynamics – galaxies: stellar content

## 1 INTRODUCTION

The stellar mass function (SMF) of galaxies - i.e., the number density of galaxies per unit of stellar mass - has become a key tool for galaxy evolution studies, as its shape and normalization are regulated by the mass assembly history of galaxies. With increasing observational data on large samples of galaxies in both the local and the high-redshift Universe, considerable efforts have been made in the quantification of the overall shape of the SMF for different population of galaxies as well as its evolution over cosmic time (e.g., Ilbert et al. 2010; Peng et al. 2010; Baldry et al. 2012; Davidzon et al. 2017). This has also made the SMF the primary tool for calibrating cosmological simulations of galaxy formation and evolution (e.g. Genel et al. 2014; Crain et al. 2015; Pillepich et al. 2018).

★ E-mail: kxguo@pku.edu.cn

The analysis of SMF is even more powerful when applied to different galaxy classes, as it encapsulates the effects of different physical processes on the mass accretion history of galaxies. Thus, providing important clues on the mass regimes within which different evolutionary paths for galaxy transformation are most likely. For instance, the comparison between SMFs for star-forming galaxies (SFG) and passive galaxies suggests a faster quenching rate in more massive galaxies (e.g., Peng et al. 2010; Ilbert et al. 2010).

Among these studies, the study of SMFs of galaxies of different morphology is a topic of particular interest, as morphological transformation is expected to be tied to galaxy evolution and accretion history intimately. Disc-like structures mostly arise from dissipational gas accretion (e.g., Fall & Efstathiou 1980), while the formation of spheroidal structures, including galaxy bulges and ellipticals, has been widely believed to be related with dissipationless mergers (e.g., Cole et al. 2000), and disk mergers also have an impact in torquing gas to lose the angular momentum in trans-

forming a galaxy from late-type to early-type (e.g., Gerhard 1981; Hernquist 1992, 1993; Heyl et al. 1994).

Several independent works have shown that the mass distribution of late-type (disk-dominated) galaxies and that of early-type (bulge-dominated) galaxies show distinct difference. The early-types dominate the population with $M_* > 10^{10}\mathrm{M}_\odot$, while the late-types are dominated at low stellar mass (Kelvin et al. 2014; Moffett et al. 2016a). Despite this, the two classes contribute nearly equally to the global stellar mass budget of the local Universe $\Omega_*$ (Driver et al. 2007; Moffett et al. 2016b). All this, would suggest that mergers play an as important role in mass assembly as gas accretion, and dominate the galaxy evolution in massive regime.

The underlying assumption of the above scenario is that, visual morphology is able to isolate truly different kinematic components, especially components like dispersion-supported bulges and rotationally-supported disks, which are directly linked to the merging history of galaxies.

While this assumption was commonly accepted in the past, the last decade has clearly shown that galaxies with distinct visual morphology can share similar kinematic properties. Most of early-type galaxies (ETGs) are found to have a rotational component (e.g., Kormendy & Bender 1996; Faber et al. 1997; Cappellari et al. 2007; Emsellem et al. 2007, 2011), arguing against that the origin of ETGs or massive galaxies as exclusively (dissipationless) mergers. Non-rotating galaxies, on the other hand, take the fraction of only $<\sim 1/3$ in total ETGs, and are found almost only in galaxies with $M_* > 10^{11}\mathrm{M}_\odot$ (van de Sande et al. 2017b; Graham et al. 2018).

Therefore, the contribution of the different physical processes in the mass assembly history of galaxies is no longer reliable. While major mergers or multiple minor dry mergers are necessary in the formation of slow rotators (SRs) (e.g., Naab et al. 2014), fast rotators (FRs) can be transformed from late-type disks following a continuous kinematic evolution (Cortese et al. 2016). Additionally, the bulge component in late-type galaxies, can be either dispersion dominated classical bulge arisen from galaxy mergers, or rotating systems originated from secular evolution of disks (Méndez-Abreu et al. 2014; Erwin et al. 2015).

The advent of integral-field spectroscopic (IFS) galaxy survey is finally helping to shed some lights on this issue, providing a more physically-motivated approach to investigate the assembly history of galaxies. Many works have just focused on the relative fraction between FRs and SRs (Cappellari 2016, and references therein), and in most cases only limited to pre-visually-classified early-type galaxies.

In this study, we take a different approach and present the first investigation of the contribution of different kinematic families of galaxies to the stellar mass function in the local Universe. Thus, in addition of presenting the first stellar mass functions for slow and fast rotators, we split fast rotators into 'dynamically cold' fast rotators (i.e., consistent with intrinsic axis ratios smaller than ~0.3) and 'composite' rotators (i.e., either tick disks or bulge plus disks objects) to determine their overall contribution to the stellar mass function. This allows us to explore the mass-dependent contribution of different physical processes to the whole population of galaxies.

This paper is structured as follows. We introduce the dataset in Section 2 and describe the feasibility of the SMF fitting method in Section 3. We show our results in Section 4 and make discussions in Section 5. A Chabrier IMF is used throughout the paper. We assume the following cosmological parameters: $\Omega_0 = 0.3, \Omega_\Lambda = 0.7, H_0 = 70\,\mathrm{km\,s^{-1}}$.

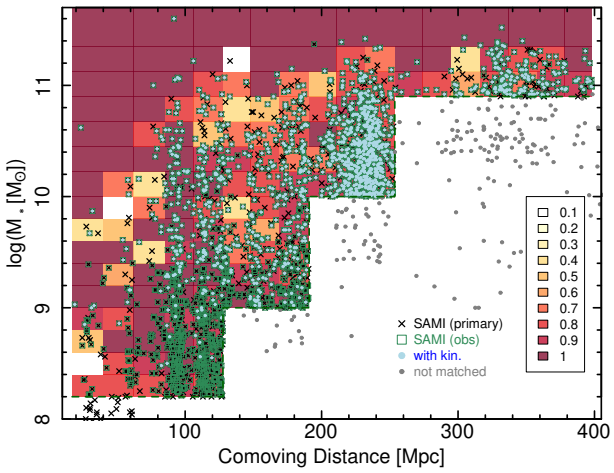


**Figure 1.** The distribution of the SAMI primary sample (*black crosses*) in the stellar mass-comoving distance plane. All galaxies observed by SAMI are labeled as *green squares*, and galaxies with available kinematics shown as *lightblue points*. *Grey points* indicate filler galaxies in the SAMI survey. The underlying grid shows the completeness of the sample in each bin of mass and distance.

## 2 DATA

Our sample is extracted from the overlap between the SAMI Galaxy Survey internal full data release (v0.11) and the Galaxy and Mass Assembly (GAMA) survey (Driver et al. 2011). The SAMI Galaxy Survey has targeted 2153 low-redshift galaxies ($z < 0.1$) in the 3 GAMA equatorial regions corresponding to an area of $144\,\mathrm{deg}^2$ in total, using the SAMI multi-object IFS instrument (Croom et al. 2012) mounted on the 3.9 metre Anglo-Australian Telescope (Bryant et al. 2015). SAMI fibres are fed to the double-beam AAOmega spectrograph (Sharp et al. 2006), providing a spectral resolutions of $R = 1812$ for the blue part (3700 – 5700Å), and $R = 4263$ for the red part (6300 – 7400Å) of the spectrum, respectively. The SAMI cubes have 50×50 0.25 $(0.5 \times 0.5)\,\mathrm{arcsec}^2$ spaxels along the spatial direction, covering the 14.7 arcsec diameter aperture of the SAMI hexabundle (Bland-Hawthorn et al. 2011; Bryant et al. 2014) and an average seeing of 2.16 arcsec. The data reduction is described in detailed in Allen et al. (2015) and Sharp et al. (2015). We refer readers to Green et al. (2018) and Scott et al. (2018) for Data Release I and II, respectively.

In this work, we focus on the 1896 galaxies included in the SAMI primary sample (i.e., excluding filler targets), in the footprint of GAMA as described in Bryant et al. (2015) , and with a lower-limit mass cut at $M_* > 10^{8.2}\mathrm{M}_\odot$ (hereafter "SAMI(obs)", *green squares* in Figure 1). As described in Bryant et al. (2015), the configuration of SAMI

plates is done to maximize the number of objects observable within a SAMI field of view, without pre-selection on morphology or environment. The stellar mass estimation is described in Bryant et al. (2015), following the method of Taylor et al. (2011). The uncertainty introduced by photometric error is around 0.05 dex, while the intrinsic scatter of color-dependent M/L is about 0.1 dex.

Visual morphology classification in SAMI has been performed taking advantage of Sloan Digital Sky Survey Data Release Nine (SDSS DR9) $gri$ color images, as discussed in Cortese et al. (2016). Despite 80 unclassified galaxies ("?") and galaxies without a consensus in morphology classification ("NA" in Figure 4), 1816 galaxies have classifications from late-type disks to ellipticals without ambiguity. Briefly, galaxies with early-type morphologies or no presence of spiral arms are classified as ETGs, and the galaxies fulfilling these conditions but having signs of star formation are excluded. ETGs with disks are further classified as S0s. Here, we constrain LTGs to be only visually pure disks/irregular galaxies and classify other late-type galaxies with intermediate types of morphologies as MTGs. Precisely, LTGs corresponds to L.S. in Figure 4, and MTGs consists of E./L.S and E.S, with ETGs including all earlier types.

Effective radii ($r_e$), ellipticities ($\epsilon$), and position angles have been derived using the Multi-Gaussian Expansion (MGE; Emsellem et al. 1994; Cappellari 2002) technique performed on SDSS $r$-band images with the code from Scott et al. (2009) and D'Eugenio et al. (in prep). Stellar kinematics are measured from the SAMI data by using the penalized pixel fitting code as described in van de Sande et al. (2017a). 1222 Galaxies in the sample have stellar kinematic information (aperture uncorrected) by the criteria as that of van de Sande et al. (2017b): signal-to-noise (S/N)>3Å$^{-1}$, $\sigma_{\rm obs}$ >FWHM$_{\rm intr}$/2 $\sim$ 35km s$^{-1}$, and $\sigma_{\rm error} < \sigma_{\rm obs} * 0.1 + 25{\rm km\,s^{-1}}$ (see van de Sande et al. 2017a) [1]. No additional cut on stellar mass or morphology or other kinematic features is applied. The spin parameter $\lambda_{\rm r_e}$ for each galaxy has been calculated according to Equation 9 in Cortese et al. (2016):

$$\lambda_R \equiv \frac{\langle R|V|\rangle}{\langle R\sqrt{V^2+\sigma^2}\rangle} = \frac{\sum_{k=1}^{n} F_k R_k |V_{k\,\rm los}|}{\sum_{k=1}^{n} F_k R_k \sqrt{V_{k\,\rm los}^2+\sigma_k^2}} \quad (1)$$

,where $n$ includes all pixels within r$_{\rm e}$.

## 3 METHOD

To derive SMFs for our sample we use the fitting tool 'dftools' (Obreschkow et al. 2018). 'dftools' provides maximum-likelihood fitting with both Schechter (Schechter 1976) and stepwise (either linear or spline) function, with over/under-density estimated and corrected automatically and iteratively. Similar to other SMF fitting method, the package estimates an effective volume for each grid of $M_*$, based on a selection function describing the ratio between the number of galaxies accounted into the fitting and that in the real universe, at given $M_*$ and redshift. However, since SAMI galaxies are selected from GAMA I survey which consists of 3 different fields (G09, G12 and G15), the over/under-density correction does not only depend on redshift but also deviate from field to field. Thus the effective volumes, i.e., the maximum volume that a galaxy can be observed after density correction, of galaxies in different fields at fixed stellar mass, are different in different fields. To address this complication, instead of running the fitting procedure to the full sample, we calculate the effective volume for individual galaxies and take them directly into the fitting. In this section, we describe our method of correcting the density inhomogeneity and the incompleteness of the sample. We also compare the SMFs derived based on this method with both that from a volume-limited sample and that from previous works.

[1] Only 28 galaxies are with r$_{\rm e}$ < HWHM$_{\rm PSF}$ and removing them does not affect our results.

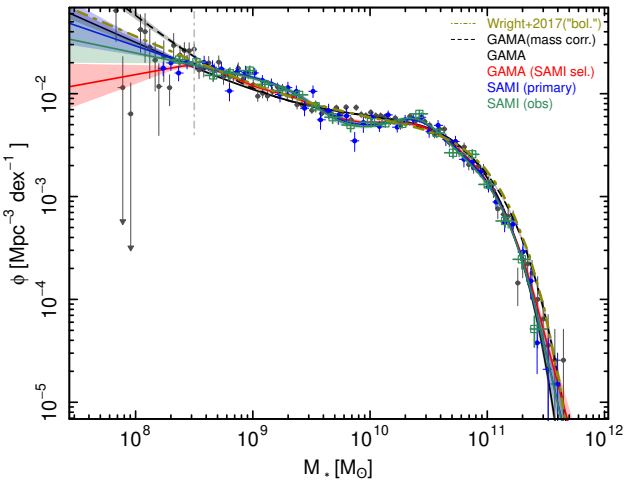


**Figure 2.** The comparison of SMFs for GAMA and SAMI galaxies obtained using different sample selections. The *black symbols* show the GAMA-I sample defined in Section§3, with the *solid and dashed black lines* show the best-fits with or without aperture corrections applied to the stellar mass. For comparison, we show the SMF from Wright et al. (2017) based on GAMA sample with MAGPHYS stellar mass estimation as the *dash-dotted olive line*. The results obtained for a SAMI-like selection applied to the GAMA-I sample, the SAMI primary sample and the SAMI observed sample are shown in red, blue and green, respectively.

### 3.1 A grid-based $V_{\rm eff}$ method

We adopt the calculation of effective volume in Baldry et al. (2012), which is equivalent to the density-corrected $V'_{\rm max}$ method in Cole (2011). Practically, we select galaxies in GAMA-I DR2 catalog(Liske et al. 2015) with $M_* > 10^{9.6} M_\odot$ (corresponding to $M_r < -18$) as the density-defining population (DDP), and the effective volume for each galaxy $i$ is given by:

$$V_{\rm eff,i} = \frac{\rho_{\rm ddp}(0.004; z_{\rm max,i})}{\rho_{\rm ddp}(0.004; 0.095)}, \quad (2)$$

where $\rho_{\rm ddp}(z_a; z_b)$ is the number density of DDP between redshift $z_a$ and $z_b$, and 0.004 and 0.095 are lower and upper redshift limits for SAMI galaxies. Given SAMI's stepped

sample selection (Figure 1), $z_{\rm max,i}$ is one of [0.004, 0.02, 0.03, 0.045, 0.06, 0.095]. It should be noted that to recover the under-densities and cosmic variance of low-redshift GAMA regions(Driver et al. 2011), we scale our derived SMFs up by a factor of 1.13. This factor is applied to match the integrated number density of galaxies with $M_* > 10^{10}{\rm M}_\odot$ with that calculated based on GAMA galaxies in the same mass range within $0.07 < z < 0.19$, the value of which is also adopted as the fiducial density in Wright et al. (2017).

Besides the galaxy distribution in real space, the incompleteness of observation is an additional factor that needs to be accounted for. A simple approach is to modify the effective volumes in grids of mass and comoving distance by multiplying the original $V_{\rm eff,i}$ by a completeness factor described by the fraction of galaxies observed in each grid, i.e., $\frac{N_{\rm obs}}{N_{\rm PS}}$, where $N_{\rm obs}$ and $N_{\rm PS}$ are the number of galaxies observed and that in SAMI primary sample, respectively. Each grid has a size of 0.2 dex × 19 Mpc. The distribution of the completeness factor is shown together with the stepwise-selected SAMI galaxies in Figure 1. The resulting SMF fitted based on SAMI (obs) sample (*green*) is shown together with that of SAMI primary sample (*blue*) in Figure 2.

When considering the reliability of reproducing SMFs based on galaxies partially selected from an original dataset, we have applied multiple experiments with artificial selection function, and compare the output SMFs with the one fit from the parent sample, which consists of galaxies between $0.004 < z < 0.095$ with $\log(M_*/{\rm M}_\odot) > 7.6 + 7.7\times10^{-3} * (r/{\rm Mpc}) - 6.6\times10^{-6} * (r/{\rm Mpc})^2$ in GAMA-I DR2 catalog (Taylor et al. 2011). The above criterion is defined from a binomial fitting to the peak value in the distribution of $M_*$ as a function of comoving distance $r$. We find that a stepwise-spline function with a proper step width [2] works better than (double) Schechter function in reproducing SMFs. That is because a stepwise-spline function has an advantage of fitting parameters independently to $M_*$ distribution in each bin, allowing a loyal representing of the real distribution rather than Schechter functions.

In Figure 2, we show the comparison between the SMF fitted by double Schechter function based on the GAMA parent sample (*black solid*), and the SMF fitted by stepwise function based on GAMA galaxies selected by the same step-series selection criteria of SAMI primary sample ("GAMA(SAMI sel.)", *red*). The difference between the two is 1% (5%) in number (mass) density for galaxies with $M_* > 10^{8.2}\,{\rm M}_\odot$. This error stemmed from the stepwise selection is numerically less than the $1\sigma$ uncertainty of fitting.

The stellar mass estimations adopted by the SAMI and GAMA surveys are slightly different, with the former based on a $g-i$ color dependent $M_*/M_i$ (Bryant et al. 2015), approximating the individually SED fitting method of Taylor et al. (2011) that have been applied to the latter. The resulting difference in SMF fitting, between SAMI primary sample ("SAMI(primary)", *blue*) and GAMA galaxies selected by SAMI selection criteria (*red*), could also be found in Figure 2. The two SMFs match each other very well for $M_* > 10^{9.2}{\rm M}_\odot$, and the deviation for less massive part causes an offset of 8% in number density but less than 1% in mass density, which is very small compared to other uncertainty contributors.

Correction of Eddington bias (Eddington 1913) is a built-in procedure in 'dftools'. However, given the low level of random noise (~ 0.05dex) in stellar mass estimation propagated from the photometric error, the uncertainty in fitting parameters caused by not considering Eddington-bias is rather small relatively to that of the fitting itself, which is estimated by Laplace approximation, equivalent to performing bootstrap iterations of resampling in most cases (for details, see Obreschkow et al. 2018).

We find a total value of $\Omega_{\rm stars} = 1.41 \pm 0.10^{+0.36}_{-0.29} \times 10^{-3}$ relative to the critical density, calculated by integrating the mass density of galaxies with $10^{8.5} < M_*/{\rm M}_\odot < 10^{12}$, where the second uncertainty components come from the systematic uncertainty of 0.1 dex on stellar mass estimation based on $g$- and $i$- band photometry (Taylor et al. 2011). The difference caused by not applying aperture correction for stellar mass estimation (*black dashed* vs. *black solid* in Figure 2) is ~ 4.4% in this mass range. Given the value of $\Omega_{\rm stars} = 1.61 \times 10^{-3}$ by integrating the "bolometric" SMF of Wright et al. (2017) in the same mass range, the difference between our value and that from other works(Wright et al. 2017, and references therein) could be mostly explained by the difference in sample selection and fitting methods.

To summarize, despite the marginal difference caused by utilizing different stellar mass catalogs, the reliability of our method in correcting the selection function and other incompleteness can be demonstrated from the consistence between the SMF estimated based on GAMA-I sample and that of galaxies observed by SAMI. Given that our main goal is to compare SMFs and contributions to $\Omega_{\rm stars}$ for different types of galaxies (i.e., relative differences), small systematic effects in the normalisation do not affect significantly our main conclusions.

### 3.2 An application on stepwise SFMs divided by morphology

We apply the above described grid-based $V_{\rm eff}$ method in deriving SMFs divided by morphology to test the feasibility of our SMFs divided by different groups. Morphological types are defined in the previous section, and include ETGs (ellipticals and S0s), MTGs (mainly early spirals), and LTGs (late spirals). The fraction of galaxies that are morphologically classified is higher than 97%. Practically, we correct this incompleteness by weighting $V_{\rm eff}$ the fraction of galaxies with certain morphologies in grids the same as that in the above subsection. Only marginal differences would be found if no correction was applied.

We show our fitting curves together with the weighted number density in Figure 3, with colored regions showing $1\sigma$ error of the best-fit curve. Consistent with what has been found in statistical studies based on visually classified morphology (e.g., Kelvin et al. 2014; Moffett et al. 2016a), from low to high stellar masses, the morphology of galaxies becomes more and more spheroidal like, with a transition mass between disk-dominated and spheroid-dominated galaxies at around $10^{10}{\rm M}_\odot$. It is hard to give a quantitative comparison with other studies, given the different techniques/datasets used to perform visual classification. However, our results qualitatively agree with the SMFs of "Spheroid Dominated"

[2] For example, the width should not be smaller than 0.1 dex in fitting a SMF based on 300 galaxies ranging from $10^9$ to $10^{12}{\rm M}_\odot$.

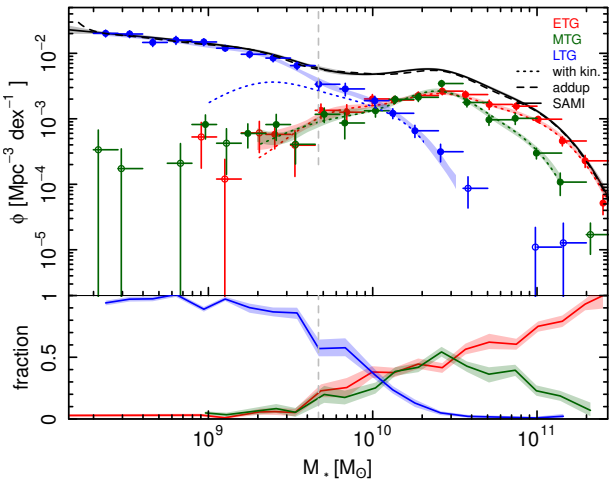


**Figure 3.** *Upper panel:* The SMFs for all our SAMI observed sample (*black solid line*), and for individual classes of visual morphology (from ETG in red to LTG in blue). We show the best-fitting function on for bins with more than 4 galaxies. The *dotted* lines show how the result would change if we include only galaxies with available kinematic information. The sum of the SMFs of all fitting curves is shown by the *black dashed line*. *Lower panel:* The lower panel shows the fraction in the number density of different classes at given stellar mass. The *vertical dashed line* shows the completeness limit in stellar mass when comparing galaxies of different kinematic type, same as that in Figure 5b.

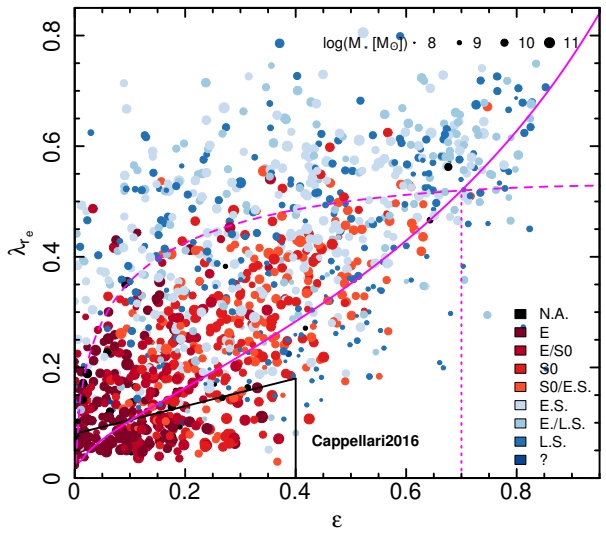


**Figure 4.** The distribution of spin parameter ($\lambda_{r_e}$) and ellipticity ($\epsilon$) for the 1222 galaxies with reliable kinematic information. Galaxies are coded by morphological type in color and stellar mass in size. The *black frame* shows the separation between fast and slow rotators defined by Cappellari (2016), while the *solid magenta line* shows the theoretical prediction for the edge-on view of galaxies with constant anisotropic factor $\delta = 0.7 \times \epsilon_{\rm intr}$(Cappellari et al. 2007). A galaxy with $\epsilon_{\rm intr} = 0.7$ viewed from different inclination angles outlines the segment between $\epsilon$ of 0 and 0.7 on the *magenta dashed line*, which is selected to be the separation between FR+s and FR-s.

and that of "Disc Dominated" in Kelvin et al. (2014) and Moffett et al. (2016a) if L.S. and E./L.S. labeled in Figure 4 are taken as "Disc Dominated" galaxies.

## 4 SMF DIVIDED BY KINEMATIC TYPES

In this section, we focus on the SMF as a function of kinematic classes to explore the mass budget of each kinematic types to the whole galaxy population, in order to figure out the contribution of different physical processes responsible for (re)shaping the stellar orbits in galaxy assembly. We use the spin parameter ($\lambda_{\rm r_e}$) and ellipticity ($\epsilon$) plane to define different families of objects. We adopt the separation between fast rotators (FR) and slow rotators (SR) from Cappellari (2016) (*black frame* in Figure 4), and we consider galaxies without available kinematic information (i.e., observed by SAMI but not full-filling the quality cuts for stellar kinematic, "nokin"s) as a separate type.

In order to distinguish FRs with low and high spin at fixed ellipticity, we use the predicted relation presented by Binney (2005)(see also Equation 14-16 in Cappellari 2016). In particular, given that the anisotropy of a FRs is bounded by a relation of the form $\delta \approx \beta_z = 0.7 \times \epsilon_{\rm intr}$ (Cappellari et al. 2007), FRs with $\lambda_{\rm r_e}$ higher than that predicted at a given $\epsilon_{\rm intr}$ are more isotropic than those below such a threshold. [3].

Thus, we use a value of $\epsilon_{\rm intr} = 1 - 0.3 = 0.7$ (*the dashed magenta line* in Figure 4) to divide 'dynamically cold' systems from slower axis-symmetric rotators. This cut is roughly consistent with the typical threshold separating visually pure disks from composite systems and/or bulges (see also Weijmans et al. 2014; Foster et al. 2017)

The plane used for our kinematics selection is shown in Figure 4, with morphological types shown in different colors. Besides a general trend from late-type dominant to early-type dominant with decreasing $\lambda_{\rm r_e}$, it is also evident that FRs consists of all morphological types, while SRs are mainly ellipticals or S0s with stellar mass greater than $10^{11}$M$_\odot$. This minority and mass preference of SRs is consistent with previous works focusing on fractions of galaxies with different kinematics (e.g., van de Sande et al. 2017b; Graham et al. 2018), and a larger portion of the mass budget from FRs compared to SRs is also expected.

In Figure 5, we compare the SMFs for all FRs and SRs (a), and for the three kinematic classes selected above (FR+, FR-, SR). The SMF for galaxies without kinematic information are plotted as *grey* lines. Due to the small number statistics of SRs, which causes the fitting not making much physical sense, we show only number densities for SRs. The frac-

[3] For detailed calculation, see Equation B1 in Emsellem et al. (2007) and Equation 12-16 in Cappellari et al. (2007). We adopt $\kappa = 1$ as the conversion factor between $V/\sigma$ and $\lambda_{\rm R}$.

tion of each population at given stellar mass is also shown in lower panels.

From Figure 5a, it is clear that the number density of FRs overwhelms SRs practically all stellar masses covered by SAMI, with SRs matching the fraction of FRs only at $> 10^{11}\mathrm{M}_{\odot}$ (see also Khochfar et al. 2011; Emsellem et al. 2011; Greene et al. 2017, 2018; van de Sande et al. 2017b). Conversely to what observed in the case of visual morphology, there is no apparent transition point in stellar mass between FR and SR classes below $10^{11.3}\mathrm{M}_{\odot}$. This difference results from the broad overlap in kinematic properties between galaxies with different morphological type, which can already be seen from Figure 4.

This difference is even more dramatic if we determine the contribution of different kinematic classes to $\Omega_*$ by integrating the SMF for different classes for $M_* > 10^{9.7}\,\mathrm{M}_{\odot}$, which roughly corresponds to the stellar mass at which our completeness in stellar kinematic drops below ~80%. We find that ~82% of the stellar mass in the local Universe is hosted in FRs, whereas only ~14% is harboured in SRs, the remaining ~7% is hosted in galaxies for which a kinematic classification was not possible.

As shown in Figure 5a, the fraction of galaxies with no kinematic information increases with decreasing stellar mass, and practically dominates our sample below $M_* \sim 10^{9.5}\,\mathrm{M}_{\odot}$. This makes it unclear that if FRs dominate the whole galaxy population down to low-mass end. To push the constraint of ratio of FRs to SRs down to $10^9\mathrm{M}_{\odot}$, we introduce the assumption that low-mass SFGs should be FRs. This is based on the expectation that star formation takes place in disks and it is suppported by the fact that SRs are expected to be produced mainly by gas-poor merger (e.g., Lagos et al. 2018a,b) and hosted by low specific-star-formation-rate (SSFR) galaxies (Naab et al. 2014).

Specifically, we assume galaxies with $\Delta(\mathrm{SFR}) = \mathrm{SFR} - \mathrm{SFMS} > -1\,\mathrm{dex}$ to be FRs, where SFR is star formation rate taken from the multi-wavelength observation based MAGPHYS catalog (Davies et al. 2016; Driver et al. 2018), and SFMS is star formation main sequence defined by a broken linear approximation [4]. The effect of this correction to the SMFs and relative fraction of FRs in our sample is shown by the blue dashed lines in Figure 5a. As expected, the fraction of FRs becomes flat down to $10^9\mathrm{M}_{\odot}$, and contribution of FRs to the stellar mass budget of the local Universe increases to 84%.

In Figure 5b, we present the SMFs and relative fractions obtained by splitting FRs into two different kinematic classes as described above. These two classes show a similar stellar mass distribution, with FR- clearly dominating in number for $M_* > 10^{10.2}\mathrm{M}_{\odot}$. Less clear is what happens for $M_* < 10^{9.7}\mathrm{M}_{\odot}$: while FRs- seem to still be the dominant population, the number of galaxies with no kinematic information becomes significant and we cannot exclude that the decrease in the SMFs of FR+ is simply an incompleteness effect. Regardless, by integrating the SMFs of the two classes we find that FR- harbor nearby a factor of ~2 more mass than FR+ (i.e., 55% vs. 27%).

[4] Our SFMS is $\log(SFR) = 0.99\log(M_*) - 9.89$ for $M_* < 10^{10}\mathrm{M}_{\odot}$, and $\log(SFR) = 0.23\log(M_*) - 2.29$ for $M_* \geq 10^{10}\mathrm{M}_{\odot}$. This agrees with Guo et al. (2015) and Popesso et al. (2019) in corresponding $\mathrm{M}_* - \mathrm{z}$ range, and the selection guarantees a fraction of > 96% galaxies with kinematic information to be FRs.

**Table 1.** The percentage of the mass budget for different classes of kinematics for galaxies.

| $f_{\Omega_{\mathrm{stars}}}(M_* > 10^{9.7}\mathrm{M}_{\odot})$ | FR | FR+ | FR- | SR | nokin |
|---|---|---|---|---|---|
| original (this work) (*solid* in Figure 5a) | 82 | 27 | 55 | 14 | 4 |
| with seeing correction (FR) (Graham et al. 2018) | 82 | 57 | 25 | 14 | 4 |
| with seeing correction (all) (Graham et al. 2018) | 88 | 57 | 31 | 8 | 4 |
| $f_{\Omega_{\mathrm{stars}}}(M_* > 10^{9}\mathrm{M}_{\odot})$ | | | | | |
| original | 79 | - | - | 14 | 7 |
| with FRs complemented (*dashed* in Figure 5a) | 84 | - | - | 14 | 2 |

Even in this case, it is interesting to compare visual morphology with kinematic classification. As shown in Figure 5b, at stellar masses where late spirals give way to the early types ($M_* \sim 10^{10}\,\mathrm{M}_{\odot}$), there is still a good fraction of dynamically cold galaxies (FR+s) which are generally visually classified as two-component galaxies. This indicates that dynamically cold galaxies defined from their kinematics are much more predominant than their morphological counterpart, i.e., the LTGs.

To test if this conclusion varies with the changing of our separation between FR+s and FR-s, we test the ratio of the number of visually classified LTGs ($\mathrm{N_{LTG}}$) and MTGs ($\mathrm{N_{MTG}}$) as a function of stellar mass and the threshold used to the define the two classes: i.e., 0.6, 0.7 (this work) and 0.8 (Figure 6). As expected, FR-s are dominated by visually classified MTGs across nearly the entire mass range investigated here ($M_* > 10^{10.2}\mathrm{M}_{\odot}$), for stellar masses greater than $\sim 10^{10}\mathrm{M}_{\odot}$ the majority of FR+s would be visually classified as MTGs. While the exact value of the ratio $\mathrm{N_{LTG}}/\mathrm{N_{MTG}}$ varies as a function of the threshold used to separate the two kinematic classes, our overall conclusions are not qualitatively affected.

A potential issue affecting our result is the effect of beam smearing on the estimate of $\lambda_{\mathrm{r_e}}$. This could artificially reduce the value of stellar spin parameter, enhancing the importance of slow rotating systems in the stellar mass budget of the local Universe. To test the potential effect of beam smearing, we apply the Sérsic-index dependent seeing correction presented by Graham et al. (2018). Although, technically, this correction is suitable only for FRs, we also check that our results do not change in case we blindly apply this correction to all our sample. The results are shown in Table 1. While, as expected, the relative contribution of FR and SR to $\Omega_*$ is almost independent of beam smearing effect, the situation is more complicated for the two classes of fast rotators. Once the Graham et al. (2018) correction is applied, the role of FR+s and FR-s is reversed, with FR+s galaxies becoming the dominant population. While this would further reinforce our argument that dynamically cold disks are way more important than what suggested by visual morphol-

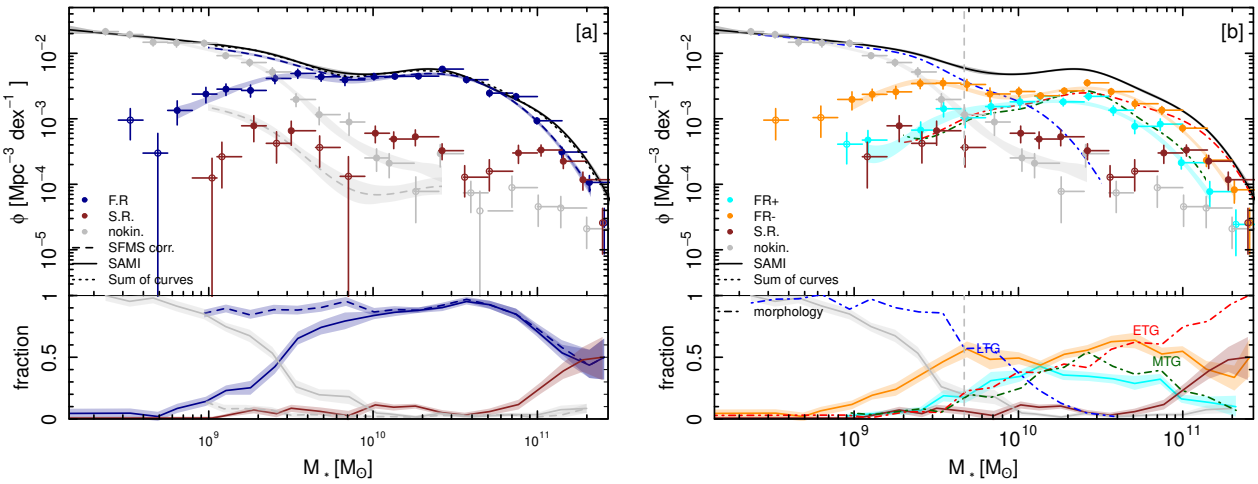


**Figure 5.** *Left.* SMFs divided by kinematic types for FRs and the number density for SRs. The *solid black* line shows the SMF for the full sample, and *gray* symbols galaxies without available kinematic information. FRs are indicated in blue and SRs in red. As in Figure 3, points are average number density in each mass bin and best-fitting curves shown only for mass bins with more than 4 galaxies The fraction between populations at given stellar mass (in logarithm) are shown in lower panels. The blue and grey dashed lines in both panels show the change introduced by assuming that all star-forming galaxies with no kinematic information are FRs. *Right*: Same as left panel, but separating FRs+ from FRs-. The fractional distribution of morphological types is also shown for reference. In both panels, the *vertical dashed line* sets a lower $M_*$ limit above which we can make an unambiguous comparison between populations.

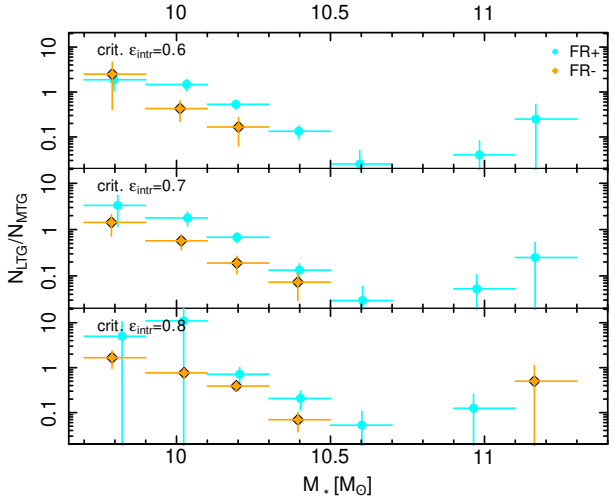


**Figure 6.** The ratio between the number of LTGs and MTGs as a function of stellar mass in groups of FR+s and FR-s, with changing $\epsilon_{\rm intr}$ in separating dynamically-cold systems from fast rotators.

ogy, the change by almost a factor of two in the contribution to $\Omega_*$ of different classes of FRs highlights the challenges in interpreting individual estimates of stellar spin at face value.

## 5 DISCUSSION AND CONCLUSION

In this paper, we have tested our ability to accurately reconstruct the SMFs for the SAMI Galaxy Survey, properly taking into account all the selection effect included in the original sample selection and during the observations. We have then quantified for the first time the SMFs for galaxies showing different stellar kinematic properties. We confirm that regular rotators the dominant population at almost all mass. FRs contribute ~ 80% to the total mass budget, with the ratio between FRs and SRs decreasing with increasing stellar mass only for $M_* > 10^{10.5}$M$_\odot$. At least one-third of the stellar mass harbored by FRs is found in systems with kinematic properties consistent with purely rotating disks, with rotators having low stellar spin starting to dominate at $M_* > 10^{10}$M$_\odot$. This is clearly in contrast with the equal contribution of spheroidal and disk components to the stellar mass budget of the local Universe as argued from visual morphology studies (Moffett et al. 2016a,b),

In our study, SRs that are believed to be mostly generated from (dissipationless) mergers (e.g., Jesseit et al. 2009; Naab et al. 2014; Lagos et al. 2018b), are confirmed to take up to only < 20% of the mass density, with most of them found in galaxies with $M_* > 10^{10.5}$M$_\odot$. This minority suggests that the processes which completely destroy ordered rotation take a small part in the mass assembly of the average galaxy in the local Universe, and only take effects on galaxies with $M_* > 10^{10.5}$M$_\odot$.

As the spin of a regular rotator is intrinsically correlated to its intrinsic ellipticity(Cappellari et al. 2007), disk thickening and the formation of a classical bulge will cause a decrease in $\lambda_{r_e}$ (e.g. Cappellari et al. 2013; Cappellari 2016, and references therein), making a galaxy move downwards in Figure 4, i.e., from the group of FR+ to FR-. Thus, the

fact that the ratio between FR-s and FR+s seems to increase with mass for $M_* > 10^{10}\mathrm{M}_\odot$ implies that the processes which efficiently thicken a disk and form a classical bulge are mostly efficient in this mass range.

It is also interesting to note that for $M_* > 10^{10}\,\mathrm{M}_\odot$, the number density of FR+s surpasses that of late spirals, with the trend of FR+ fraction with a stellar mass similar to that of MTGs (typical two-component galaxies) in morphology. While works based on visual morphology suggests that a stellar mass of $\sim 10^{10}\,\mathrm{M}_\odot$ is a transition mass between bulge- and disk-dominant galaxies, our results seem to imply that many galaxies which are morphologically classified as multiple component systems including a "bulge" are still as dynamically cold as late-type spirals. In other words, a significant fraction of the two-component galaxies are disks in kinematics. The FR+ fraction decrease for stellar masses larger than $\sim 10^{10.5}\,\mathrm{M}_\odot$, most likely because of the increasing emergence of both disk thickening and/or the dissipationless processes creating classical bulges and/or SRs.

Lastly, we remind the reader that our classification of FR+s/FR-s, i.e., dynamically-cold/two-component disks, is based on the distribution of $\lambda_{\mathrm{r_e}}$ as a function of $\epsilon$ of galaxies, without applying any kinematic decomposition of the velocity field such as those introduced by Tabor et al. (2017) and Rizzo et al. (2018). The next steps for this type of studies is to start separating different kinematic components within galaxies and to quantify their contribution to the stellar mass budget in the local Universe. This should provide better constraints to the different physical processes regulating the mass growth of galaxies as, at this stage, we are admittedly sensible only to processes significantly perturbing the global stellar velocity fields. Given that both observational (Tabor et al. 2017, 2019; Rizzo et al. 2018) and theoretical (Scannapieco et al. 2010; Martig et al. 2012; Wang et al. 2019; Zhu et al. 2018) work have clearly shown that photometric and kinematic decomposition do not always agree, we cannot blindly rely on previous works based on 2D bulge-to-disk decomposition if we aim at improving our reconstruction of the accretion histories of nearby galaxies.

## ACKNOWLEDGEMENTS

We acknowledge the helpful discussions with Dr. Angus Wright. K.G. acknowledges the support from the Beijing Natural Science Foundation (Youth program) under grant no.1184015. Parts of this research were supported by the Australian Research Council Centre of Excellence for All Sky Astrophysics in 3 Dimensions (ASTRO 3D), through project number CE170100013. This research is also supported jointly by China National Postdoctoral Science Foundation (No. 2017M610696), China Scholarship Council and the International Centre for Radio Astronomy Research. LC is the recipient of an Australian Research Council Future Fellowship (FT180100066) funded by the Australian Government. JvdS is funded under Bland-Hawthorn's ARC Laureate Fellowship (FL140100278).

The SAMI Galaxy Survey is based on observations made at the Anglo-Australian Telescope. The Sydney-AAO Multi-object Integral field spectrograph (SAMI) was developed jointly by the University of Sydney and the Australian Astronomical Observatory. The SAMI input catalogue is based on data taken from the Sloan Digital Sky Survey, the GAMA Survey and the VST ATLAS Survey. The SAMI Galaxy Survey is supported by the Australian Research Council Centre of Excellence for All Sky Astrophysics in 3 Dimensions (ASTRO 3D), through project number CE170100013, the Australian Research Council Centre of Excellence for All-sky Astrophysics (CAASTRO), through project number CE110001020, and other participating institutions. The SAMI Galaxy Survey website is http://samisurvey.org/ .

## REFERENCES

Allen, J. T., Croom, S. M., Konstantopoulos, I. S., et al. 2015, MNRAS, 446, 1567
Baldry, I. K., Driver, S. P., Loveday, J., et al. 2012, MNRAS, 421, 621
Bland-Hawthorn, J., Bryant, J., Robertson, G., et al. 2011, Optics Express, 19, 2649
Binney, J. 2005, MNRAS, 363, 937
Bryant, J. J., Bland-Hawthorn, J., Fogarty, L. M. R., Lawrence, J. S., & Croom, S. M. 2014, MNRAS, 438, 869
Bryant, J. J., Owers, M. S., Robotham, A. S. G., et al. 2015, MNRAS, 447, 2857
Cappellari, M. 2002, MNRAS, 333, 400
Cappellari, M., Emsellem, E., Bacon, R., et al. 2007, MNRAS, 379, 418
Cappellari, M., McDermid, R. M., Alatalo, K., et al. 2013, MNRAS, 432, 1862
Cappellari, M. 2016, Annual Review of Astronomy and Astrophysics, 54, 597
Cole, S., Lacey, C. G., Baugh, C. M., & Frenk, C. S. 2000, MNRAS, 319, 168
Cole, S. 2011, MNRAS, 416, 739
Cortese, L., Fogarty, L. M. R., Bekki, K., et al. 2016, MNRAS, 463, 170
Crain, R. A., Schaye, J., Bower, R. G., et al. 2015, MNRAS, 450, 1937
Croom, S. M., Lawrence, J. S., Bland-Hawthorn, J., et al. 2012, MNRAS, 421, 872
Davidzon, I., Ilbert, O., Laigle, C., et al. 2017, A&A, 605, A70
Davies, L. J. M., Driver, S. P., Robotham, A. S. G., et al. 2016, MNRAS, 461, 458
Driver, S. P., Allen, P. D., Liske, J., & Graham, A. W. 2007, ApJ, 657, L85
Driver, S. P., Hill, D. T., Kelvin, L. S., et al. 2011, MNRAS, 413, 971
Driver, S. P., Andrews, S. K., da Cunha, E., et al. 2018, MNRAS, 475, 2891.
Eddington, A. S. 1913, MNRAS, 73, 359
Emsellem, E., Monnet, G., & Bacon, R. 1994, A&A, 285, 723
Emsellem, E., Cappellari, M., Krajnović, D., et al. 2007, MNRAS, 379, 401
Emsellem, E., Cappellari, M., Krajnović, D., et al. 2011, MNRAS, 414, 888.
Erwin, P., Saglia, R. P., Fabricius, M., et al. 2015, MNRAS, 446, 4039
Faber, S. M., Tremaine, S., Ajhar, E. A., et al. 1997, AJ, 114, 1771
Fall, S. M., & Efstathiou, G. 1980, MNRAS, 193, 189
Foster, C., van de Sande, J., D'Eugenio, F., et al. 2017, MNRAS, 472, 966.
Genel, S., Vogelsberger, M., Springel, V., et al. 2014, MNRAS, 445, 175
Gerhard, O. E. 1981, MNRAS, 197, 179

Graham, M. T., Cappellari, M., Li, H., et al. 2018, MNRAS, 477, 4711
Green, A. W., Croom, S. M., Scott, N., et al. 2018, MNRAS, 475, 716
Greene, J. E., Leauthaud, A., Emsellem, E., et al. 2017, ApJ, 851, L33.
Greene, J. E., Leauthaud, A., Emsellem, E., et al. 2018, ApJ, 852, 36.
Guo, K., Zheng, X. Z., Wang, T., et al. 2015, ApJ, 808, L49.
Hernquist, L. 1992, ApJ, 400, 460
Hernquist, L. 1993, ApJ, 409, 548
Heyl, J. S., Hernquist, L., & Spergel, D. N. 1994, ApJ, 427, 165
Ilbert, O., Salvato, M., Le Floc'h, E., et al. 2010, ApJ, 709, 644
Jesseit, R., Cappellari, M., Naab, T., Emsellem, E., & Burkert, A. 2009, MNRAS, 397, 1202
Kelvin, L. S., Driver, S. P., Robotham, A. S. G., et al. 2014, MNRAS, 444, 1647
Khochfar, S., Emsellem, E., Serra, P., et al. 2011, MNRAS, 417, 845.
Kormendy, J., & Bender, R. 1996, ApJ, 464, L119
Lagos, C. del P., Stevens, A. R. H., Bower, R. G., et al. 2018, MNRAS, 473, 4956
Lagos, C. del P., Schaye, J., Bahé, Y., et al. 2018, MNRAS, 476, 4327.
Liske, J., Baldry, I. K., Driver, S. P., et al. 2015, MNRAS, 452, 2087.
Martig, M., Bournaud, F., Croton, D. J., et al. 2012, ApJ, 756, 26
Méndez-Abreu, J., Debattista, V. P., Corsini, E. M., & Aguerri, J. A. L. 2014, A&A, 572, A25
Moffett, A. J., Ingarfield, S. A., Driver, S. P., et al. 2016, MNRAS, 457, 1308
Moffett, A. J., Lange, R., Driver, S. P., et al. 2016, MNRAS, 462, 4336
Naab, T., Oser, L., Emsellem, E., et al. 2014, MNRAS, 444, 3357
Obreschkow, D., Murray, S. G., Robotham, A. S. G., & Westmeier, T. 2018, MNRAS, 474, 5500
Peng, Y.-j., Lilly, S. J., Kovač, K., et al. 2010, ApJ, 721, 193
Pillepich, A., Springel, V., Nelson, D., et al. 2018, MNRAS, 473, 4077
Popesso, P., Concas, A., Morselli, L., et al. 2019, MNRAS, 483, 3213
Rizzo, F., Fraternali, F., & Iorio, G. 2018, MNRAS, 476, 2137
Scannapieco, C., Gadotti, D. A., Jonsson, P., et al. 2010, MNRAS, 407, L41
Scott, N., Cappellari, M., Davies, R. L., et al. 2009, MNRAS, 398, 1835
Scott, N., van de Sande, J., Croom, S. M., et al. 2018, MNRAS, 481, 2299
Schechter, P. 1976, ApJ, 203, 297
Sharp, R., Saunders, W., Smith, G., et al. 2006, Proc. SPIE, 6269, 62690G
Sharp, R., Allen, J. T., Fogarty, L. M. R., et al. 2015, MNRAS, 446, 1551
Tabor, M., Merrifield, M., Aragón-Salamanca, A., et al. 2017, MNRAS, 466, 2024
Tabor, M., Merrifield, M., Aragón-Salamanca, A., et al. 2019, MNRAS, 485, 1546
Taylor, E. N., Hopkins, A. M., Baldry, I. K., et al. 2011, MNRAS, 418, 1587
Wang, L., Obreschkow, D., Lagos, C. del P., et al. 2019, MNRAS, 482, 5477
Weijmans, A.-M., de Zeeuw, P. T., Emsellem, E., et al. 2014, MNRAS, 444, 3340.
Wright, A. H., Robotham, A. S. G., Driver, S. P., et al. 2017, MNRAS, 470, 283
van de Sande, J., Bland-Hawthorn, J., Fogarty, L. M. R., et al. 2017, ApJ, 835, 104
van de Sande, J., Bland-Hawthorn, J., Brough, S., et al. 2017, MNRAS, 472, 1272.
Zhu, L., van de Ven, G., Méndez-Abreu, J., et al. 2018, MNRAS, 479, 945